Ultrafast Science
A SCIENCE PARTNER JOURNAL

RESEARCH ARTICLE

Two-Beam Ultrafast Laser Scribing of Graphene Patterns with 90-nm Subdiffraction Feature Size

Xi Chen[1,2*] and Min Gu[1,2*]

[1]Institute of Photonic Chips, University of Shanghai for Science and Technology, Shanghai 200093, China.
[2]Centre for Artificial-Intelligence Nanophotonics, School of Optical-Electrical and Computer Engineering, University of Shanghai for Science and Technology, Shanghai 200093, China.

*Address correspondence to: xichen@usst.edu.cn (X.C.); gumin@usst.edu.cn (M.G.)

Citation: Chen X and Gu M. Two-Beam Ultrafast Laser Scribing of Graphene Patterns with 90-nm Subdiffraction Feature Size. *Ultrafast Sci.* 2022;2022:Article 0001. https://doi.org/10.34133/ultrafastscience.0001

Submitted 19 May 2022
Accepted 19 October 2022
Published 15 December 2022

The fabrication of high-resolution laser-scribed graphene devices is crucial to achieving large surface areas and thus performance breakthroughs. However, since the investigation mainly focuses on the laser-induced reduction of graphene oxide, the single-beam scribing provides a tremendous challenge to realizing subdiffraction features of graphene patterns. Here, we present an innovative 2-beam laser scribing pathway for the fabrication of subdiffraction graphene patterns. First, an oxidation reaction of highly reduced graphene oxide can be controllably driven by irradiation of a 532-nm femtosecond laser beam. Based on the oxidation mechanism, a 2-beam laser scribing was performed on graphene oxide thin films, in which a doughnut-shaped 375-nm beam reduces graphene oxide and a spherical 532-nm ultrafast beam induces the oxidation of laser-reduced graphene oxide. The spherical beam turns the highly reduced graphene oxide (reduced by the doughnut-shaped beam) to an oxidized state, splitting the laser-scribed graphene oxide line into 2 subdiffraction featured segments and thus forming a laser-scribed graphene/oxidized laser-scribed graphene/laser-scribed graphene line. Through the adjustment of the oxidation beam power, the minimum linewidth of laser-scribed graphene was measured to be 90 nm. Next, we fabricated patterned supercapacitor electrodes containing parallel laser-scribed graphene lines with subdiffraction widths and spacings. An outstanding gravimetric capacitance of 308 F/g, which is substantially higher than those of reported graphene-based supercapacitors, has been delivered. The results offer a broadly accessible strategy for the fabrication of high-performance graphene-based devices including high-capacity energy storage, high-resolution holograms, high-sensitivity sensors, triboelectric nanogenerators with high power densities, and artificial intelligence devices with high neuron densities.

Introduction

Recently, scientists have found that graphene, a layered structure of carbon atoms tightly packed into 2-dimensional honeycomb lattices, demonstrates extraordinary electrical, optical, and mechanical properties [1–5]. Patterned graphene structures have been demonstrated to be capable of significantly improving the performances of devices including energy storage [6–9], holograms [10–12], sensors [13–15], and triboelectric nanogenerators [16–18]. Among various graphene-based materials, graphene oxide (GO), which is a skeleton of graphene decorated with epoxide, carbonyl, hydroxyl, and phenol functional groups, has attracted considerable interest [19,20].

For the fabrication procedure of patterned GO-based devices, first, large-scale production of aqueous GO colloids is realized by chemical graphite with strong oxidizers and acids, and then GO films are deposited by spin-coating, drop-casting, blade, or freezing-drying method. Next, a single-beam laser scribing procedure drives the elimination of the functional groups and a subsequent reduction from GO films to patterns of laser-scribed graphene oxide (LSG) [21–23]. The dimensional parameters of the patterns determine the surface areas of the devices and thus the performances [24,25]. Consequently, subdiffraction featured LSG patterns hold the key to the performance breakthrough of the devices. Currently, the linewidths of the reported LSG patterns fabricated by the single-beam pathway were microsized [26–28]. It is a tremendous challenge to achieve features of LSG patterns beyond the diffraction limit barrier.

Recently, a 2-beam laser scribing technology has been reported using a doughnut-shaped beam to inhibit the photopolymerization triggered by the writing beam at the doughnut ring, thereby fabricating resin patterns with linewidths far beyond diffraction limits [29], gyroid patterns with 350-nm feature size [30], and reduced GO patterns with microsized features [31]. However, since the inhibition pathway of GO photoreduction has not been realized, the technology to fabricate subdiffraction featured LSG patterns has not been developed. In this paper, an oxidation reaction of highly reduced GO driven by a femtosecond laser beam irradiation has been demonstrated. A 2-beam laser scribing of LSG patterns with a minimum linewidth of 90 nm has been realized. The subdiffraction featured patterns deliver an extremely high gravimetric capacitance of 308 F/g, around 50% higher than those for reported graphene supercapacitors.

Materials and Methods

Preparation of GO thin films

GO was prepared from graphite powder by a modified Hummers' method. First, graphite and $NaNO_3$ were mixed with concentrated H_2SO_4 under stirring, followed by the addition of $KMnO_4$. Then, H_2O_2 was added at 98 °C. The GO suspension was obtained after the centrifugation. Aqueous GO suspensions were spin-coated on the polyethylene terephthalate (PET) films with a thickness of 0.2 mm, and then GO thin films with different thicknesses were produced.

Subdiffraction laser fabrication and characterization of LSG patterns

A continuous-wave mode laser (Coherent-cube) with a wavelength of 375 nm was adopted as the doughnut-shaped GO reduction beam. The beam was expanded after going through a half-wave plate, modulated by a phase plate (vortex phase, RPC Photonics Inc.) to generate a focus profile with zero intensity at the center of the focal region, and then introduced into a high numerical aperture objective (NA = 1.4, Olympus). A femtosecond laser (Coherent Chameleon) with a wavelength of 532 nm was used as the GO oxidation beam. Confocal detector photomultiplier tubes were used for the system alignment and the beam overlapping. The exposure of these concentric beams was simultaneously controlled by synchronized shutters and monitored by a charge-coupled device camera. Raman measurements were performed with Bruker Dimension Icon-Raman atomic force microscopy (AFM). X-ray diffraction (XRD) spectra were measured with Philips X'Pert materials research diffractometry (MRD). X-ray photoelectron spectroscopy (XPS) measurement was conducted with Kratos AXIS Supra XPS. The features and the cross-sectional profiles of the fabricated structures were measured with Zeiss Supra 40 VP field emission scanning electron microscopy (SEM) and Bruker Dimension Icon-Raman AFM. Before the SEM measurement, the sample was deposited with a 6-nm gold layer in a thermal evaporator. Fourier transform infrared (FTIR) spectroscopy was used with Nicolet 6700 FTIR.

Supercapacitor assembly and characterization

The PET films were put into a thermal evaporator. The film edges were deposited by a 100-nm Au layer pattern for electron collection. Next, aqueous GO suspensions were spin-coated on the PET films, and then reduced graphene oxide (rGO) thin films with thicknesses of 200 and 850 nm were produced. The LSG patterns were fabricated in the middle of the films using the 2-beam laser scribing, with areas of 9 mm^2. For the assembly with a solid-state gel electrolyte, a solution of polyvinyl alcohol/phosphoric acid (PVA/H_3PO_4) was prepared by adding 3 ml of H_3PO_4 and 5 g of PVA into 40 ml of deionized water at 85 °C for 2 h under continuous stirring. The PVA/H_3PO_4 electrolyte was drop cast above the LSG patterns and solidified for 24 h. Two LSG electrodes were separated by ion-porous separators (CelgardR 3501) and sealed by parafilm for electrochemical measurements. The electrochemical performances of the supercapacitors were investigated by galvanostatic charge/discharge (GCD), cyclic voltammetry (CV), and electrochemical impedance spectroscopy (EIS) measurement using Gamry Interface 1000 Potentiostat. The gravimetric capacitance (C_g) was calculated by the following formula: $C_g = I\Delta t/\Delta V$, where I is the discharge current density calculated by the mass of the electrode including LSG lines and interspaces, Δt is the discharge time, and ΔV is the discharge potential drop.

Results and Discussion

Threshold model of 2-beam graphene laser scribing

The 2-beam laser scribing procedure to fabricate subdiffraction patterned graphene structures is schematically illustrated in Fig. 1. Unlike the polymer-based resin patterns, what we control during the 2-beam fabrication is a reversible reduction–oxidation reaction, rather than a one-way polymerization. A doughnut-shaped 375-nm beam and a spherical 532-nm beam are concentric and simultaneously controlled. Because the outer diameter of the doughnut-shaped beam is larger than the diameter of the spherical beam, at the beginning GO is reduced to LSG by the front half of the doughnut-shaped beam. Next, the spherical beam turns LSG to oxidized LSG (OLSG), splitting the LSG line into 2 subdiffraction featured segments. Due to the interlayer expansion, OLSG changes slightly during the second-round photoreduction from the rear half of the doughnut-shaped beam. Consequently, a subdiffraction LSG/OLSG/LSG line can be fabricated.

The rate equation of the laser-driven LSG oxidation was established.

$$-\frac{dA_{carbon}}{dt} = kA_{carbon}^{b} \tag{1}$$

Here, A_{carbon} is the carbon concentration of the LSG film, k is the rate constant, and b is the reaction order. Since k is a function of the oxidation laser beam power (P), once the scanning speed is fixed Eq. 1 can be converted to:

$$\Delta A_{carbon} = f(P) \cdot A_{carbon}^{b} \tag{2}$$

Here, ΔA_{carbon} is the carbon concentration change during oxidation.

The generation of the OLSG line occurs as the oxidation laser beam power (P) exceeds the oxidation threshold (P_{th}). Due to the intensity distribution of the Gaussian beam, the relationship between P and P_{th} is given by:

$$P_{th} = Pe^{\frac{-L_{OLSG}^2}{2w_0^2}} \tag{3}$$

Here, W_0 is the beam diameter. Consequently, the OLSG linewidth (L_{OLSG}) can be written as:

$$L_{OLSG} = \alpha\sqrt{\ln\left(\frac{P}{P_{th}}\right)} \tag{4}$$

α is a constant once the beam diameter is fixed. The LSG linewidth (L_{LSG}) then reads:

$$L_{LSG} = \frac{\beta - \alpha\sqrt{\ln\left(\frac{P}{P_{th}}\right)}}{2} \tag{5}$$

Here, β is the LSG linewidth without the application of the oxidation beam.

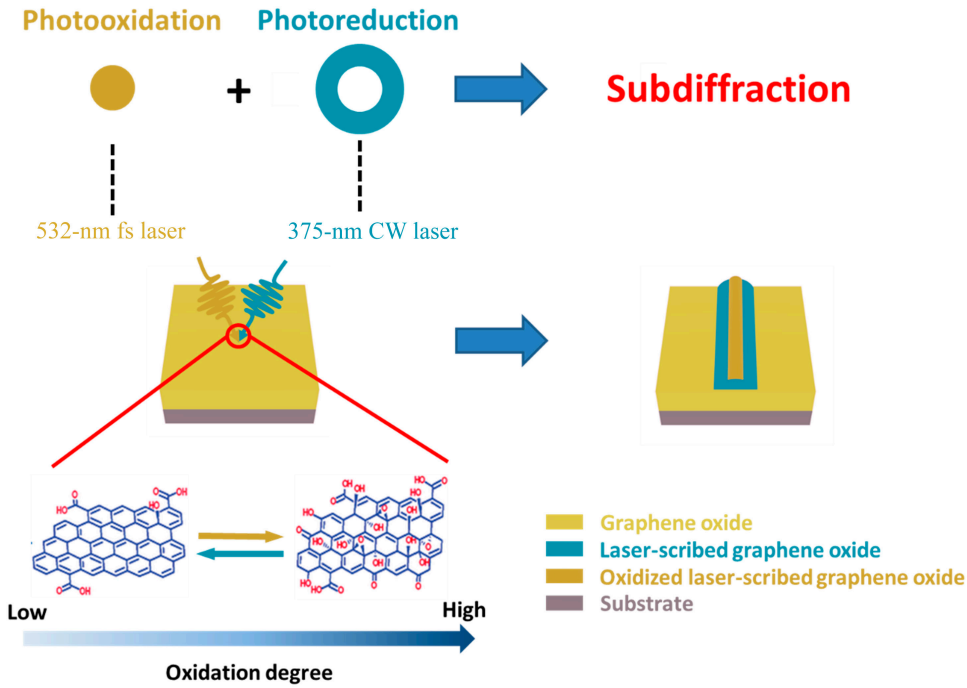

Fig. 1. The 2-beam laser scribing procedure to fabricate subdiffraction graphene structures. fs, femtosecond; CW, continuous wave.

Laser-driven GO reduction and LSG oxidation

To demonstrate the laser-driven reactions of GO and LSG, we measured Raman spectra of laser-treated GO films and calculated the intensity ratio between the peaks D and G (I_D/I_G), which are used to characterize the LSG reduction degrees. Figure 2A shows the relationship between the laser powers and the intensity ratios during GO reduction under a scanning speed of 10 μm/s. The ratio reduction occurs under powers of 6, 9, and 12 mW. In this case, the ratio values decline with the laser power increase due to the enhancement of the reduction degrees. Once the power is above 12 mW, laser ablation turning GO to carbon dioxide is induced.

LSG with high reduction degrees can be oxidized by the irradiation of a 532-nm femtosecond laser beam, as shown in Fig. 2B. Under an 18-mW power and a 10 μm/s scanning speed of the oxidation beam, the intensity ratio enhances from 0.29 to 0.86 (the purple line in Fig. 2B), indicating that oxygen molecules act as oxidizing agents turning LSG to OLSG [32,33]. The laser ablation happens when the power is above 18 mW. XRD results also confirm the LSG oxidation through the intensity increase of the (001) diffraction peak and the decrease of the (002) peak (Fig. S1). On the contrary, the LSG film with a relatively high I_D/I_G ratio of 0.71 is further reduced when the power is below 6 mW (black line). The film with a ratio of 0.47 is oxidized under powers of 3 and 6 mW, while it is reduced under 9, 12, and 15 mW. Regarding the second-round reduction by the 375-nm beam, the OLSG film with an intensity ratio of 0.86 is slightly reduced since the ratio changes to 0.65 under a 9-mW power (Fig. 2C). The I_D/I_G ratio decrease of the GO reduction is sharper than that of OLSG because of the interlayer expansion during the laser scribing procedures.

The mechanism of photooxidation driven by the 532-nm beam was investigated by the chemical composition change of LSG as a function of the beam power. According to XPS data shown in Fig. 2D and Fig. S2, in the LSG film with a 0.29 intensity ratio, a significant increase in the concentrations and peak intensities of hydroxyl (286 eV) and epoxide (289 eV) groups and a decrease in carbon bonds (284 eV) can be observed. Moreover, compared with the FTIR spectroscopy of LSG, that of OLSG displays an obvious presence of O–H bonds at 3,300 cm^{-1} (Fig. S3). These trends demonstrating the LSG oxidation are consistent with that of the Raman data (Fig. 2B). Once the oxidation power is higher than 9 mW, a linear relationship between the carbon concentration and the oxidation power can be observed. It can be fitted with Eq. 2: $\Delta A_{carbon} = f(P) \cdot A^{b}_{carbon}$, in which $f(P)$ is a linear function and the reaction order (b) is zero. Regarding the LSG film with a 0.47 I_D/I_G ratio, the Raman results (Fig. 2B) imply that the 532-nm beam treatment of LSG leads to a balancing act between oxidation and reduction, and the oxidation is prone to be triggered on the LSG film under low beam powers. Slight oxidation occurs within a beam power from 3 to 9 mW, mainly due to the generation of hydroxyl groups. A further increase of the power induces a break of the carbon–oxygen bonds and thus the reduction of the LSG (Fig. S4).

The relationship between the laser powers and the intensity ratios under a high scanning speed of 15 μm/s was also studied (Fig. S5, A to C). GO photoreduction is induced once the 375-nm laser power is below 21 mW. The threshold is higher than that under a 10 μm/s speed because of the less energy received by the GO film under the same beam power. The LSG film with the highest reduction degree can be oxidized by the 532-nm beam. The 15-mW beam increases the I_D/I_G ratio from 0.3 to 0.73. Under the powers of 18 and 21 mW, the intensity ratios of OLSG are lower than that under 12 mW. We also found slight changes in the intensity ratios during the second-round photoreduction. Once a low scanning speed of 5 μm/s is applied (Fig. S6, A to C), through the illumination of the 532-nm beam, the I_D/I_G ratio can increase from 0.59 to 0.64 due to the LSG photooxidation. The threshold is lower than those under 5 and 10 μm/s speeds.

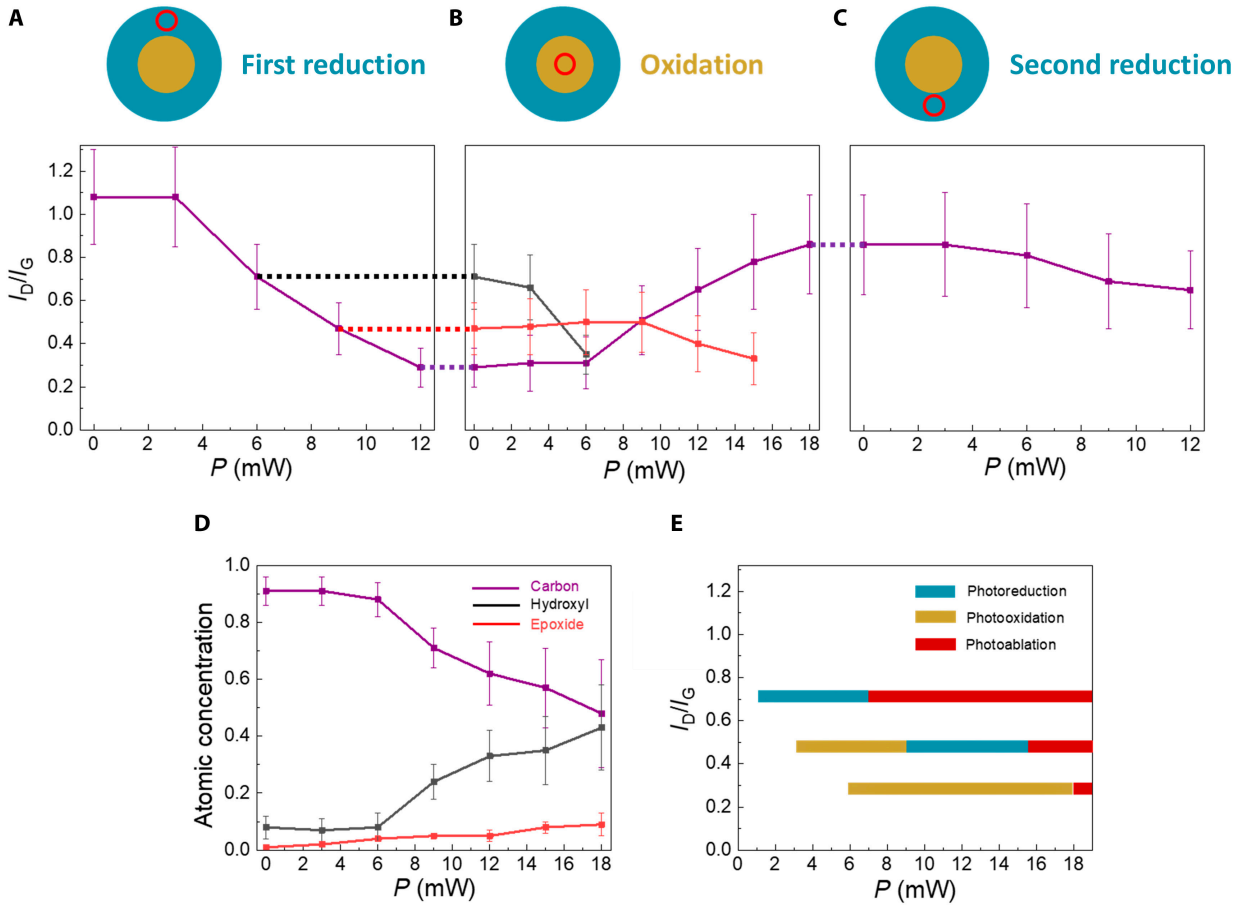

Fig. 2. Laser-driven GO reduction and LSG oxidation. The relationship between the laser powers and the intensity ratios under a scanning speed of 10 μm/s during the first reduction (A), the oxidation (B), and the second reduction (C). (D) Chemical composition changes of LSG with an I_D/I_G ratio of 0.29 treated under various oxidation beam powers. (E) Laser power ranges of LSG oxidation, reduction, and ablation under various I_D/I_G ratios and a scanning speed of 10 μm/s.

Figure 2E demonstrates the laser power ranges of LSG oxidation, reduction, and ablation under various I_D/I_G ratios and a scanning speed of 10 μm/s. LSG films with ratios of 0.29 and 0.47 can be oxidized under powers of 6 to 18 mW and 3 to 9 mW, respectively. A high scanning speed of 15 μm/s leads to a shift of the power range from 9 to 21 mW when the intensity ratio is 0.3 (Fig. S7), while under a low scanning speed of 5 μm/s the oxidation power range from 4 to 7 mW can be observed with a ratio of 0.59 (Fig. S8). Taking advantage of the power windows of the LSG oxidation, we can split a laser-scribed LSG line through the generation of OLSG and thus realize subdiffraction featured LSG patterns.

Laser-scribed LSG and OLSG patterns with subdiffraction features

To demonstrate the subdiffraction featured patterns, we conducted a 2-beam laser fabrication procedure of a 200-nm GO film by using a reduction beam and an oxidation beam introduced into a high numerical aperture objective (NA = 1.4, Olympus). LSG lines with various widths and spacings were fabricated by moving the film, while the *XY* positions of the focal spot were fixed. Without the oxidation beam, the GO reduction and the LSG formation are driven once the laser power is between the reaction threshold and the ablation threshold. The widths of the free-standing LSG line increase with the increment of the reduction beam powers (Fig. 3A and Fig. S9). Under a scanning speed of 10 μm/s, the average widths are 260 and 420 nm when the powers of the 375-nm beam are 6 and 12 mW, respectively.

While the oxidation beam is introduced, an OLSG line can be observed to emerge from the middle of the LSG line (Fig. 3B), allowing the line to be split into 2 segments. When the oxidation powers increase from 9 to 18 mW, the average widths of the OLSG lines are experimentally enhanced from 140 to 240 nm under a scanning speed of 10 μm/s, respectively (Fig. 3, B to D). Both the reduction and the oxidation beam can lead to humps with heights of 250 nm due to the interlayer expansion of the graphene-based film (Fig. 3, E and F). The OLSG linewidth results can be fitted with the following formula: $L_{OLSG} = \alpha\sqrt{\ln\left(\frac{P}{P_{th}}\right)}$ (Eq. 4), with α = 230 nm, P defined as the oxidation beam power, and P_{th} of 6 mW defined as the LSG oxidation threshold. In the meantime, the widths of the LSG lines are measured to be 140 nm under 9 mW. A minimum width of 90 nm is observed under 18 mW. The relationship between the subdiffraction linewidths and the oxidation powers agrees with the following equation: $L_{LSG} = \frac{\beta - \alpha\sqrt{\ln\left(\frac{P}{P_{th}}\right)}}{2}$ (Eq. 5), with β of 420 nm as the LSG width without the oxidation beam introduction. The material modification is mainly driven by direct photochemical

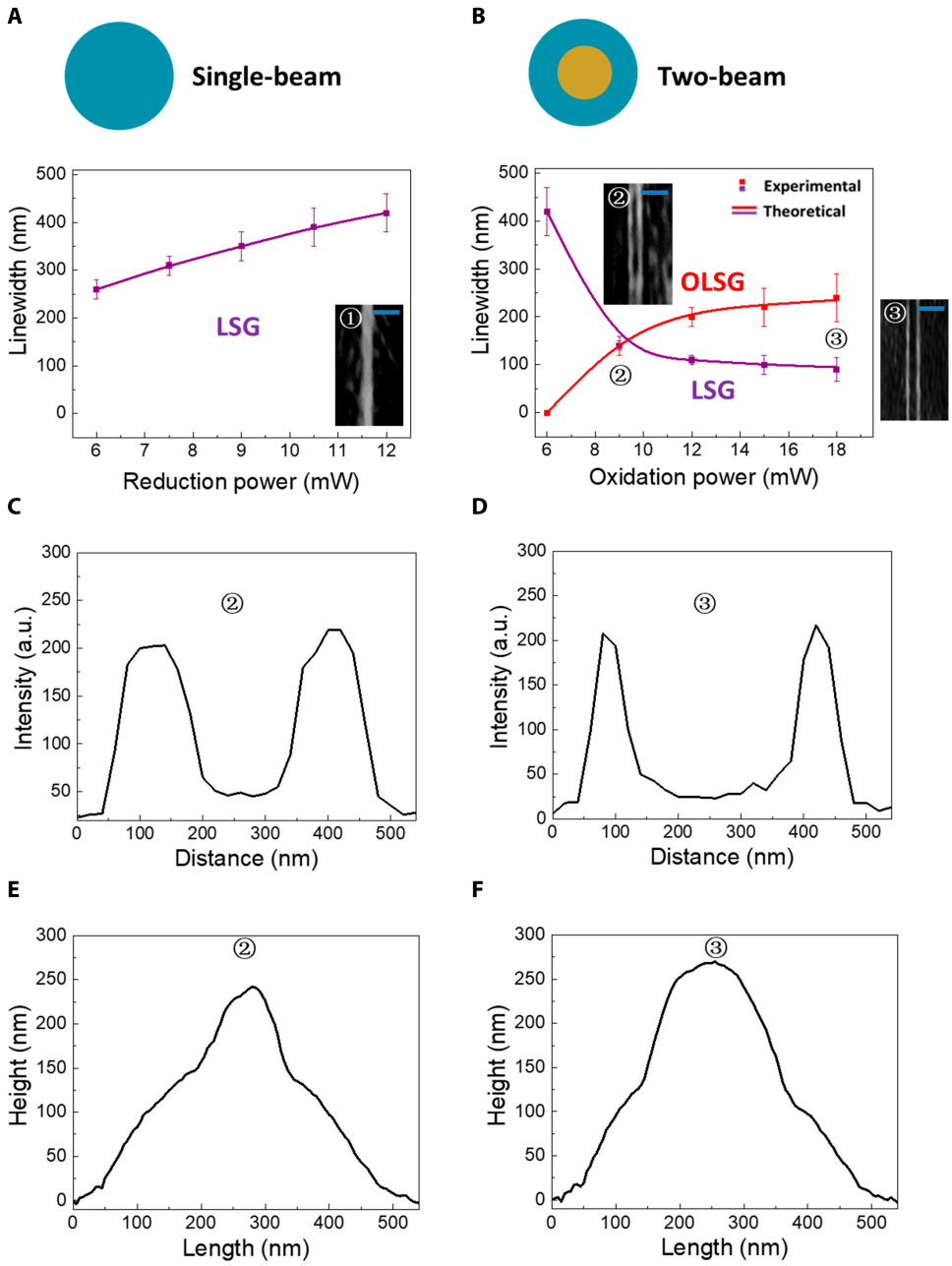

Fig. 3. Laser-scribed graphene lines with subdiffraction features. (A) Single-beam fabrication of a 200-nm GO film. The relationship between the LSG linewidths and the reduction beam powers under a 10 μm/s scanning speed, and a SEM image of the LSG line. (B) Two-beam fabrication of the 200-nm film. The experimental and theoretical relationship between the LSG/OLSG linewidths and the oxidation beam powers, and SEM images of the graphene structures. The SEM cross-sectional profiles of the structures fabricated under oxidation powers of 9 mW (C) and 18 mW (D). a.u., arbitrary units. The AFM height profiles of the structures fabricated under oxidation powers of 9 mW (E) and 18 mW (F). Scale bar: 1 μm.

reactions. The ultrashort pulse of the femtosecond laser beam scribing can suppress the thermal diffusion effect because the OLSG linewidth is significantly less than the beam diameter $(\frac{2\lambda}{\pi NA})$.

Similar subdiffraction featured structures were observed under a scanning speed of 15 μm/s. With a reduction beam of 21 mW, the average widths of the OLSG lines are 140, 200, and 240 nm when oxidation beam powers are 15, 18, and 21 mW, respectively. The results lead to LSG lines with widths of 180, 150, and 130 nm (Fig. S10). However, under a scanning speed of 5 μm/s, what we observed is not LSG, but OLSG lines only. In this case, the OLSG widths exceed those of the LSG line due to the thermal diffusion effect of the 532-nm beam.

The 2-beam laser fabrication procedure was also conducted on the 850-nm GO film. Without the oxidation beam and under a scanning speed of 10 μm/s, the average widths of the LSG lines are 310 and 550 nm when the powers of the 375-nm beam are 6 and 12 mW, respectively (Fig. S11). An OLSG line can be observed once the oxidation beam is introduced. When the oxidation powers are 9 and 18 mW, the average widths of the OLSG lines are 190 and 290 nm, and the average LSG widths

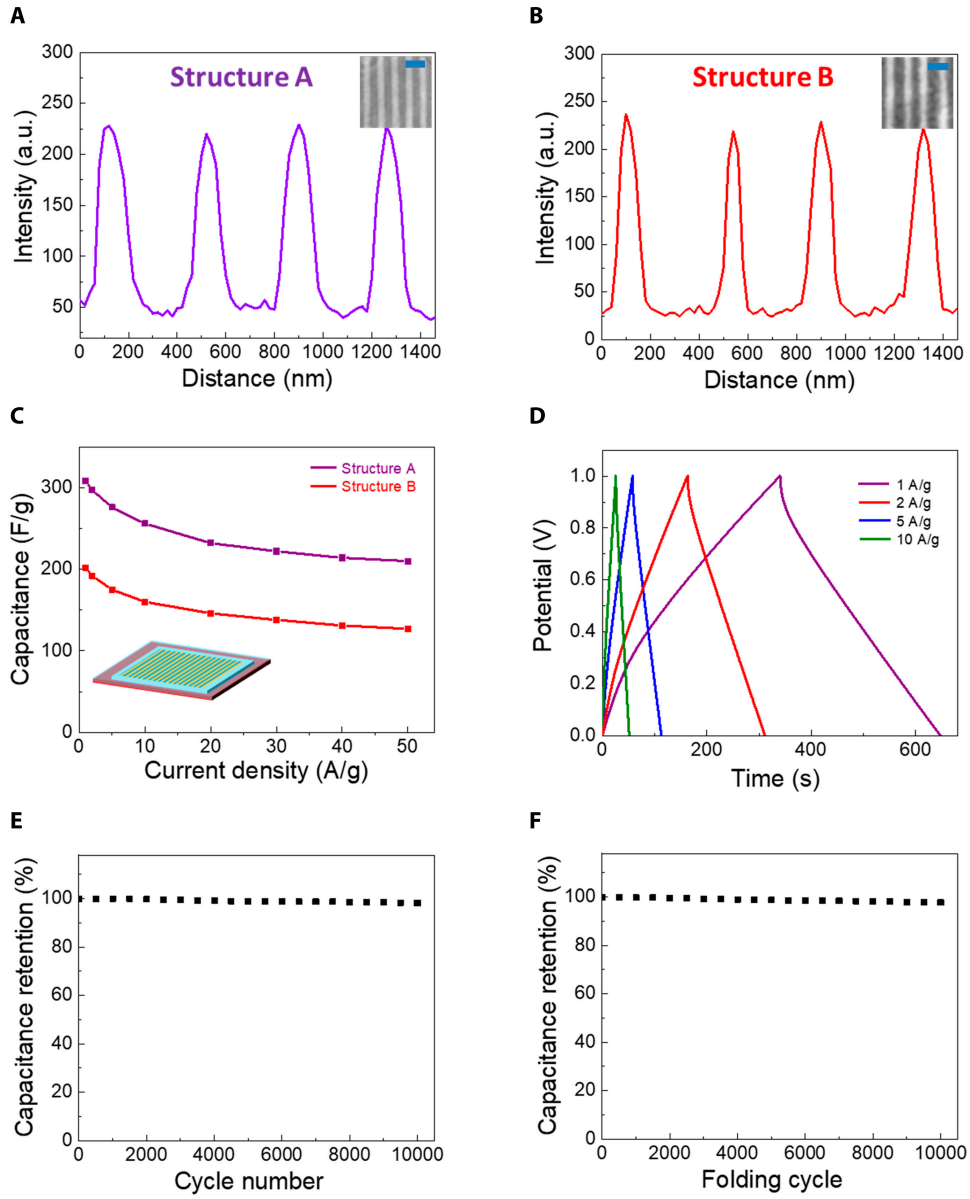

Fig. 4. Subdiffraction featured graphene patterns and electrochemical performances of supercapacitors. SEM images and profiles of LSG patterns with widths of 180 nm (A) and 130 nm (B). Scale bar: 500 nm. (C) Gravimetric capacitances of supercapacitors of graphene patterns under different current densities. Inset: The graphene pattern structure, in which a gold film (red frame) was deposited at the substrate edge and located below the GO film. (D) GCD curves of supercapacitors with the structure A electrode at different current densities. Capacitance retention of supercapacitors with the structure A electrode in 10,000 charge/discharge cycles (E) and 10,000 folding cycles (F) under a current density of 1 A/g.

are 180 and 130 nm, respectively (Fig. S12). We calculated the axial to lateral ratio of the 550-nm LSG line through a 45° tilt SEM measurement [9]. The ratio is around 1.2, indicating that the LSG is not throughout the film thickness.

Fabrication of subdiffraction featured graphene patterns and supercapacitor performances

Next, we fabricated patterns of parallel LSG lines with subdiffraction features through the 2-beam laser scribing. The parallel LSG lines with fixed distances were sequentially fabricated by moving the GO film, while the positions of both beam spots were fixed. As shown in Fig. 4 (A and B), when the 850-nm GO film was scribed under a scanning speed of 10 μm/s, parallel LSG lines with average linewidths of 180 nm (structure A) and 130 nm (structure B) were produced. The average spacings (widths of OLSG lines) are 190 and 290 nm, respectively. Through the fabrication of the 200-nm GO film, an LSG structure with a 140-nm average width and a 140-nm average spacing can be achieved under an oxidation power of 9 mW (structure C), and another structure with a 90-nm average width and a 240-nm average spacing can be realized under 18-mW power (structure D), as shown in Fig. S13. The results imply that the 2-beam laser scribing procedure can fabricate LSG patterns with features beyond the diffraction limit barrier and thus has the potential to provide performance breakthroughs for graphene-based devices.

To measure the capacity performances of the graphene electrodes, we fabricated the LSG parallel-line structures based on

the subdiffraction featured graphene structures as supercapacitor electrodes, which were assembled using a solid-state gel electrolyte of PVA/H_3PO_4. The square-shaped electrode area is fixed to be 9 mm^2. As shown in Fig. 4C, the 800-nm GO film can be fabricated to electrodes with high supercapacitor performances. On the other hand, the 200-nm film leads to significant exfoliation of the graphene flakes from the substrate, thereby resulting in lower capacitances. Structure A demonstrates the highest volumetric capacitance among the 4 structures (Fig. S14). Gravimetric capacitances of 308 and 210 F/g were measured at current densities of 1 and 50 A/g, respectively. Moreover, nearly symmetric triangle curves can be exhibited in the GCD measurements of the structure A electrodes (Fig. 4D), and the CV studies of the electrodes show quasi-rectangular loops (Fig. S15). The characteristics demonstrate an ideal electrical double layer behavior. The superior capacitance can also be verified by the EIS measurement, in which an equivalent series resistance could be derived to be only 1.1 Ω (Fig. S16).

On the other hand, the capacitance of structure A is higher than that of supercapacitors with planer LSG electrodes (212 F/g under 1 A/g current density), which were fabricated by the GO film using the reduction beam only. Once the LSG linewidth is less than the thickness and comparable with the spacing, the subdiffraction featured structures exhibit more surface areas than the planer one. A decrease of the linewidths with subwavelength features induces an exponential growth of the surface areas [34]. Consequently, the subdiffraction featured graphene structure exhibits a dramatically high gravimetric capacitance. The value is around 50% higher than those for reported graphene supercapacitors and also higher than those of some doped graphene supercapacitors (Table S1) [8,35–47]. It verifies that the subdiffraction featured structures provide performance breakthroughs for energy storage.

Moreover, excellent cycling stabilities of the subdiffraction featured graphene structures have been demonstrated. The initial capacitance retention of the supercapacitors with structures A and B after 10,000 cycles was observed to be 98.2% and 97.9% at a current density of 1 A/g, respectively (Fig. 4E and Fig. S17). The stability performances are higher than those of supercapacitors with LSG electrodes [48]. On the other hand, the supercapacitors also show high stability in mechanical cycling. The capacitance retentions are around 97.8% and 96.9% after 10,000 folding cycles at a current density of 1 A/g, respectively (Fig. 4F and Fig. S18). The 2-beam laser scribing procedure could offer a powerful and broadly feasible strategy for the fabrication of super-resolution structures and thus the realization of high-performance supercapacitors, holograms, sensors, and triboelectric nanogenerators. Moreover, artificial intelligence devices have drawn tremendous attention in neuromorphic computing due to the advantages of parallel multitasks and low energy consumption [49]. The 2-beam procedure has great potential to achieve artificial intelligence devices with high neuron densities and thus provide breakthroughs in computing power and intelligence power.

Conclusion

In summary, here, an innovative 2-beam laser scribing pathway for the fabrication of subdiffraction graphene patterns is presented. We have demonstrated that an oxidation reaction of highly reduced GO can be driven by a femtosecond laser beam irradiation. Under an 18-mW power and a 10 μm/s scanning speed of the oxidation beam, the intensity ratio between the Raman peaks D and G enhances from 0.29 to 0.86. Based on the photooxidation mechanism, a doughnut-shaped reduction laser beam and a spherical oxidation 532-nm beam are simultaneously controlled for the fabrication. The spherical beam turns LSG to OLSG, splitting the LSG line into 2 subdiffraction featured segments. A minimum LSG linewidth of 90 nm was achieved. Next, supercapacitor electrodes of subdiffraction featured patterns consisting of parallel LSG lines have been scribed. The pattern with a linewidth of 180 nm and a spacing of 190 nm delivers an extremely high gravimetric capacitance of 308 F/g, significantly high than those for reported graphene supercapacitors. The results pave the way toward high-performance graphene-based devices, especially artificial intelligence devices with high neuron densities.

Acknowledgments

Funding: This work is supported by the National Natural Science Foundation of China (grant no. 11974247), the Shanghai Science & Technology Commission (21DZ1100500), and the Shanghai Municipal Science and Technology Major Project.
Author contributions: X.C. and M.G. proposed the idea of subdiffraction laser scribing in GO films and completed the writing of the paper. X.C. performed the experiments.
Competing interests: The authors declare that they have no competing interests.

Data Availability

The data that support the findings of this study are available from the corresponding author upon reasonable request.

Supplementary Materials

Fig. S1. XRD spectra of GO, LSG with an I_D/I_G ratio of 0.29, and OLSG with an I_D/I_G ratio of 0.86.
Fig. S2. XPS spectra of GO, LSG with an I_D/I_G ratio of 0.29, and OLSG with an I_D/I_G ratio of 0.86.
Fig. S3. FTIR spectra of GO, LSG with an I_D/I_G ratio of 0.29, and OLSG with an I_D/I_G ratio of 0.86.
Fig. S4. Chemical composition changes of LSG with an I_D/I_G ratio of 0.47 treated under various oxidation beam powers.
Fig. S5. The relationship between the laser powers and the intensity ratios under a scanning speed of 15 μm/s.
Fig. S6. The relationship between the laser powers and the intensity ratios under a scanning speed of 5 μm/s.
Fig. S7. Laser power ranges of LSG oxidation, reduction, and ablation under various I_D/I_G ratios and a scanning speed of 15 μm/s.
Fig. S8. Laser power ranges of LSG oxidation, reduction, and ablation under various I_D/I_G ratios and a scanning speed of 5 μm/s.
Fig. S9. Single-beam laser fabrication of a 200-nm GO film.
Fig. S10. Two-beam laser fabrication of a 200-nm GO film.
Fig. S11. Single-beam laser fabrication of the 850-nm GO film.
Fig. S12. Two-beam laser fabrication of the 850-nm GO film.
Fig. S13. SEM images of LSG patterns.
Fig. S14. Gravimetric capacitances of supercapacitors of graphene patterns.
Fig. S15. A CV profile of the supercapacitor with structure A pattern under a scanning rate of 1 V/s.

Fig. S16. Nyquist plot of the supercapacitor with the structure A electrode.
Fig. S17. Capacitance retention of supercapacitors with the structure B electrode in 10,000 charge/discharge cycles under a current density of 1 A/g.
Fig. S18. Capacitance retention in 10,000 folding cycles of supercapacitors with the structure B electrode under a current density of 1 A/g.
Table S1. List of the capacitances of graphene and doped graphene supercapacitors.

References

1. Novoselov KS, Geim AK, Morozov SV, Jiang D, Zhang Y, Dubonos SV, Grigorieva IV, Firsov AA. Electric field effect in atomically thin carbon films. *Science*. 2004;306(5696):666–669.
2. Geim AK. Graphene: Status and prospects. *Science*. 2009;324(5934):1530−1534.
3. El-Kady MF, Shao YL, Kaner RB. Graphene for batteries, supercapacitors and beyond. *Nat Rev Mater*. 2016;1(7):16033.
4. Andrei EY, MacDonald AH. Graphene bilayers with a twist. *Nat Mater*. 2020;19(12):1265–1275.
5. Kong W, Kum H, Bae SH, Shim J, Kim H, Kong L, Meng Y, Wang K, Kim C, Kim J. Path towards graphene commercialization from lab to market. *Nat Nanotechnol*. 2019;14(10):927–938.
6. Yuan Y, Jiang L, Li X, Zuo P, Xu C, Tian M, Zhang X, Wang S, Lu B, Shao C, et al. Laser photonic-reduction stamping for graphene-based micro-supercapacitors ultrafast fabrication. *Nat Commun*. 2020;11(1):6185.
7. Xiao J, Zhan H, Wang X, Xu ZQ, Xiong Z, Zhang K, Simon GP, Liu JZ, Li D. Electrolyte gating in graphene-based supercapacitors and its use for probing nanoconfined charging dynamics. *Nat Nanotechnol*. 2020;15(8):683–689.
8. Zhu Y, Murali S, Stoller MD, Ganesh KJ, Cai W, Ferreira PJ, Pirkle A, Wallace RM, Cychosz KA, Thommes M, et al. Carbon-based supercapacitors produced by activation of graphene. *Science*. 2011;332(6037):1537–1541.
9. Wan Z, Chen X, Gu M. Laser scribed graphene for supercapacitors. *Opto-Electron Adv*. 2021;4(7):200079.
10. Chen Y, Hu P, Huang Z, Wang J, Song H, Chen X, Lin X, Wu T, Tan X. Significant enhancement of the polarization holographic performance of photopolymeric materials by introducing graphene oxide. *ACS Appl Mater Interfaces*. 2021;13(23):27500–27512.
11. Li X, Ren H, Chen X, Liu J, Li Q, Li C, Xue G, Jia J, Cao L, Sahu A, et al. Athermally photoreduced graphene oxides for three-dimensional holographic images. *Nat Commun*. 2015;6:6984.
12. Li X, Zhang Q, Chen X, Gu M. Giant refractive-index modulation by two-photon reduction of fluorescent graphene oxides for multimode optical recording. *Sci Rep*. 2013;3:2819.
13. Stanford MG, Zhang C, Fowlkes JD, Hoffman A, Ivanov IN, Rack PD, Tour JM. High-resolution laser-induced graphene. flexible electronics beyond the visible limit. *ACS Appl Mater Interfaces*. 2020;12(9):10902–10907.
14. Sun B, McCay RN, Goswami S, Xu Y, Zhang C, Ling Y, Lin J, Yan Z. Gas-permeable, multifunctional on-skin electronics based on laser-induced porous graphene and sugar-templated elastomer sponges. *Adv Mater*. 2018;30(50):e1804327.
15. Tao LQ, Tian H, Liu Y, Ju ZY, Pang Y, Chen YQ, Wang DY, Tian XG, Yan JC, Deng NQ, et al. An intelligent artificial throat with sound-sensing ability based on laser induced graphene. *Nat Commun*. 2017;8:14579.
16. Pace G, Serri M, del Rio Castillo AE, Ansaldo A, Lauciello S, Prato M, Pasquale L, Luxa J, Mazánek V, Sofer Z, et al. Nitrogen-doped graphene based triboelectric nanogenerators. *Nano Energy*. 2021;87:106173.
17. Stanford MG, Li JT, Chyan Y, Wang Z, Wang W, Tour JM. Laser-induced graphene triboelectric nanogenerators. *ACS Nano*. 2019;13(6):7166–7174.
18. Luo J, Fan FR, Jiang T, Wang Z, Tang W, Zhang C, Liu M, Cao G, Wang ZL. Integration of micro-supercapacitors with triboelectric nanogenerators for a flexible self-charging power unit. *Nano Res*. 2015;8:3934–3943.
19. Huang NM, Lim HN, Chia CH, Yarmo MA, Muhamad MR. Simple room-temperature preparation of high-yield large-area graphene oxide. *Int J Nanomedicine*. 2011;6:3443–3448.
20. Marcano DC, Kosynkin DV, Berlin JM, Sinitskii A, Sun Z, Slesarev A, Alemany LB, Lu W, Tour JM. Improved synthesis of graphene oxide. *ACS Nano*. 2010;4(8):4806–4814.
21. Lin J, Peng Z, Liu Y, Ruiz-Zepeda F, Ye R, Samuel EL, Yacaman MJ, Yakobson BI, Tour JM. Laser-induced porous graphene films from commercial polymers. *Nat Commun*. 2014;5:5714.
22. Ye R, James DK, Tour JM. Laser-induced graphene: From discovery to translation. *Adv Mater*. 2019;31(1):e1803621.
23. Ye R, James DK, Tour JM. Laser-induced graphene. *Acc Chem Res*. 2018;51(7):1609–1620.
24. Hooch Antink W, Choi Y, Seong K-d, Kim JM, Piao Y. Recent progress in porous graphene and reduced graphene oxide-based nanomaterials for electrochemical energy storage devices. *Adv Mater Interfaces*. 2018;5(5):Article 1701212.
25. Liang L, Feng Z, Zhang Q, Cong TD, Wang Y, Qin X, Yi Z, Ang MJY, Zhou L, Feng H, et al. Continuous-wave near-infrared stimulated-emission depletion microscopy using downshifting lanthanide nanoparticles. *Nat Nanotechnol*. 2021;16(6):975–980.
26. Beckham JL, Li JT, Stanford MG, Chen W, McHugh EA, Advincula PA, Wyss KM, Chyan Y, Boldman WL, Rack PD, et al. High-resolution laser-induced graphene from photoresist. *ACS Nano*. 2021;15(5):8976–8983.
27. El-Kady MF, Kaner RB. Scalable fabrication of high-power graphene micro-supercapacitors for flexible and on-chip energy storage. *Nat Commun*. 2013;4:1475.
28. Shen D, Zou G, Liu L, Zhao W, Wu A, Duley WW, Zhou YN. Scalable high-performance ultraminiature graphene micro-supercapacitors by a hybrid technique combining direct writing and controllable microdroplet transfer. *ACS Appl Mater Interfaces*. 2018;10(6):5404–5412.
29. Gan Z, Cao Y, Evans RA, Gu M. Three-dimensional deep sub-diffraction optical beam lithography with 9 nm feature size. *Nat Commun*. 2013;4:2061.
30. Gan Z, Turner MD, Gu M. Biomimetic gyroid nanostructures exceeding their natural origins. *Sci Adv*. 2016;2(5):e1600084.
31. Lamon S, Wu Y, Zhang Q, Liu X, Gu M. Nanoscale optical writing through upconversion resonance energy transfer. *Sci Adv*. 2021;7(9):eabe2209.
32. Mitoma N, Nouchi R, Tanigaki K. Photo-oxidation of graphene in the presence of water. *J Phys Chem C*. 2013;117(3):1453–1456.
33. Koivistoinen J, Sládková L, Aumanen J, Koskinen P, Roberts K, Johansson A, Myllyperkiö P, Pettersson M. From seeds to islands: Growth of oxidized graphene by two-photon oxidation. *J Phys Chem C*. 2016;120(39):22330–22341.

34. Chen X, Luan H, Gu M. Beyond high-voltage capacitors: Supercapacitor arrays based on laser-scribed subwavelength-featured graphene patterns. *ACS Appl Energy Mater*. 2022;5(8):9315–9323.
35. Zhang X, Sui Z, Xu B, Yue S, Luo Y, Zhan W, Liu B. Mechanically strong and highly conductive graphene aerogel and its use as electrodes for electrochemical power sources. *J Mater Chem*. 2011;21(18):6494−6497.
36. Zhang L, Shi G. Preparation of highly conductive graphene hydrogels for fabricating supercapacitors with high rate capability. *J Phys Chem C*. 2011;115(34):17206−17212.
37. Sheng K-X, Xu Y-X, Li C, Shi G-Q. High-performance self-assembled graphene hydrogels prepared by chemical reduction of graphene oxide. *New Carbon Mater*. 2011;26(1):9−15.
38. Ning G, Fan Z, Wang G, Gao J, Qian W, Wei F. Gram-scale synthesis of nanomesh graphene with high surface area and its application in supercapacitor electrodes. *Chem Commun*. 2011;47:5976−5978.
39. Zhang LL, Zhao X, Stoller MD, Zhu Y, Ji H, Murali S, Wu Y, Perales S, Clevenger B, Ruoff RS. Highly conductive and porous activated reduced graphene oxide films for high-power supercapacitors. *Nano Lett*. 2012;12(4):1806–1812.
40. Luan VH, Tien HN, Hoa LT, Hien NTM, Oh E-S, Chung J, Kim EJ, Choi WM, Kong B-S, Hur SH. Synthesis of a highly conductive and large surface area graphene oxide hydrogel and its use in a supercapacitor. *J Mater Chem A*. 2013;1:208−211.
41. Xu Y, Chen C-Y, Zhao Z, Lin Z, Lee C, Xu X, Wang C, Huang Y, Shakir MI, Duan X. Solution processable holey graphene oxide and its derived macrostructures for high-performance supercapacitors. *Nano Lett*. 2015;15(7):4605−4610.
42. Bai Y, Yang X, He Y, Zhang J, Kang L, Xu H, Shi F, Lei Z, Liu Z-H. Formation process of holey graphene and its assembled binder-free film electrode with high volumetric capacitance. *Electrochimica Acta*. 2016;187:543−551.
43. Huo J, Zheng P, Wang X, Gou S. Three-dimensional sulphur/nitrogen co-doped reduced graphene oxide as high-performance supercapacitor binder-free electrodes. *Appl Surf Sci*. 2018;442:575−580.
44. Chen Y, Liu Z, Sun L, Lu Z, Zhuo K. Nitrogen and sulfur co-doped porous graphene aerogel as an efficient electrode material for high performance supercapacitor in ionic liquid electrolyte. *J Power Sources*. 2018;390:215−223.
45. Ramabadran U, Ryan G, Zhou X, Farhat S, Manciu F, Tong Y, Ayler R, Garner G. Reduced graphene oxide on nickel foam for supercapacitor electrodes. *Materials (Basel)*. 2017;10(11):1295.
46. Chen Y, Li Y, Yao F, Peng C, Cao C, Feng Y, Feng W. Nitrogen and fluorine co-doped holey graphene hydrogel as a binder-free electrode material for flexible solid-state supercapacitors. *Sustain Energy Fuels*. 2019;3:2237–2245.
47. Jia S, Zang J, Tian P, Zhou S, Cai H, Tian X, Wang Y. A 3-D covalently crosslinked N-doped porous carbon/holey graphene composite for quasi-solid-state supercapacitors. *Microporous Mesoporous Mater*. 2020;293:109796.
48. Shao Y, Li J, Li Y, Wang H, Zhang Q, Kaner RB. Flexible quasi-solid-state planar micro-supercapacitor based on cellular graphene films. *Mater Horiz*. 2017;4:1145−1150.
49. Goi E, Zhang Q, Chen X, Luan H, Gu M. Perspective on photonic memristive neuromorphic computing. *PhotoniX*. 2020;1(1):3.